



LAWRENCE  
LIVERMORE  
NATIONAL  
LABORATORY

# Experimental investigation of bright spots in broadband, gated x-ray images of ignition-scale implosions on the National Ignition Facility

M. A. Barrios, S. P. Regan, L. J. Suter, S. Glenn, L. R. Benedetti, D. K. Bradley, G. W. Collins, R. Epstein, B. A. Hammel, G. A. Kyrala, N. Izumi, T. Ma, H. Scott, V. A. Smalyuk

January 8, 2013

Physics of Plasmas

## **Disclaimer**

---

This document was prepared as an account of work sponsored by an agency of the United States government. Neither the United States government nor Lawrence Livermore National Security, LLC, nor any of their employees makes any warranty, expressed or implied, or assumes any legal liability or responsibility for the accuracy, completeness, or usefulness of any information, apparatus, product, or process disclosed, or represents that its use would not infringe privately owned rights. Reference herein to any specific commercial product, process, or service by trade name, trademark, manufacturer, or otherwise does not necessarily constitute or imply its endorsement, recommendation, or favoring by the United States government or Lawrence Livermore National Security, LLC. The views and opinions of authors expressed herein do not necessarily state or reflect those of the United States government or Lawrence Livermore National Security, LLC, and shall not be used for advertising or product endorsement purposes.

# **Experimental investigation of bright spots in broadband, gated x-ray images of ignition-scale implosions on the National Ignition Facility**

M.A. Barrios<sup>1</sup>, S.P. Regan<sup>2</sup>, L. J.Suter<sup>1</sup>, S. Glenn<sup>1</sup>, L. R. Benedetti<sup>1</sup>, D. K. Bradley<sup>1</sup>,  
G. W. Collins<sup>1</sup>, R. Epstein<sup>2</sup>, B. A. Hammel<sup>1</sup>, G.A. Kyrala,<sup>3</sup> N. Izumi<sup>1</sup>, T. Ma<sup>1</sup>, H. Scott<sup>1</sup>,  
V. A. Smalyuk<sup>1</sup>

<sup>1</sup>Lawrence Livermore National Laboratory, Livermore, California 94550, USA

<sup>2</sup>Laboratory for Laser Energetics, University of Rochester 250 East River Road,  
Rochester, NY 14623-199, USA

<sup>3</sup>Los Alamos National Laboratory, Los Alamos, New Mexico, 87545, USA

## **Abstract**

Bright spots in the hot spot intensity profile of gated x-ray images of ignition-scale implosions at the National Ignition Facility (NIF)<sup>1,2</sup> are observed. X-ray images of cryogenic layered capsules and symmetry capsules (Symcap) were recorded along the hohlraum symmetry axis. The bright spots result from the heterogeneous mixing of ablator material and fuel into the hot spot by hydrodynamic instabilities, increasing the radiative cooling of the hot spot.<sup>3-5</sup> In this study Fourier analysis of the x-ray images is used to filter the bright spot signal from the low order spatial intensity envelope of the hot spot to quantify the bright spot power and to characterize the evolution of bright spots in both  $x$ - and  $k$ -space. Bright spot images were azimuthally binned to characterize bright spot location relative to known isolated defects on the capsule surface. A strong

correlation is observed between bright spot location and the fill tube for both Symcap and layered targets, indicating the fill tube is a significant seed for the ablation front instability causing hot-spot mix. The fill tube is the predominant seed for Symcaps, while other capsule non-uniformities are dominant seeds for the layered targets. A comparison of the bright spot power observed with a Si- or a Ge-doped ablator is used to study the source of hot-spot mix mass from the various target layers.

## I. INTRODUCTION

The National Ignition Facility (NIF) is a 1.8 MJ laser system irradiating targets with 192 beams of 351nm light.<sup>1,2</sup> Targets are composed of a spherical capsule placed inside a high Z hohlraum, driven by an nearly blackbody x-ray flux with a peak radiation temperature  $T_r \sim 300$  eV, generated by the hohlraum after laser irradiation of the inner wall.<sup>3</sup> The outer capsule layer composed of a low Z-material is ablated outward by the x-ray irradiation of its surface and implodes the capsule via the rocket effect. Quasi-isentropic compression of the deuterium-tritium (DT) fuel (or tritium-hydrogen-deuterium fuel, THD) is achieved by a sequence of well timed shock waves, designed to keep the fuel at a low adiabat.<sup>6,7</sup>

Target performance relies on the symmetric implosion of this highly compressed fuel, resulting in the formation of a central hot spot with high enough areal density ( $> 0.3$  g/cm<sup>2</sup>) and temperature ( $> 5$  keV) to trigger ignition and burn.<sup>8</sup> Optimal performance of these targets requires mitigating high mode perturbations ( $\ell \sim 300\text{--}2000$ ;  $\lambda \sim 20\mu\text{m}\text{--}2\mu\text{m}$ ) that develop in the outer and inner surfaces of the target and at the interfaces between the capsule layers.<sup>5</sup> Figure 1 shows a cross-section of the Rev. 5 cryogenic DT (THD)

capsule.<sup>3</sup> The capsule is composed of a plastic ablator with various levels of germanium or silicon doping, designed to minimize the growth of hydrodynamic instabilities and prevent fuel preheat. The innermost layer of the capsule is composed of solid 50/50 DT (72/22/6 THD) ice surrounding the DT (THD) gas. Surrogate capsules used to investigate implosion symmetry (Symcaps) have the same ablator configuration as cryogenic DT capsules, with a mass-equivalent layer of plastic replacing the solid DT ice, and are filled with a mixture of He and D<sub>2</sub> gas instead of DT gas. All of the capsules require a fill tube with outer diameter  $\sim 10\mu\text{m}$  connected to a  $\sim 5\mu\text{m}$  diameter hole in the ablator, as shown in Figure 1. Surface roughness and imperfections in the outer and inner surfaces of these capsules, as well as isolated defects such as the fill tube, can seed perturbations. Hydrodynamic simulations show that high mode perturbations will introduce jets of material, both from the ablator as well as cold DT, into the hot spot. The enhanced radiative cooling by the higher Z material mixed into the hot spot degrades the target neutron yield.<sup>3-5,9,10</sup> Higher Z material introduced into the hot spot will ionize and emit both x-ray continuum (free-free  $\propto Z^2$  and free-bound  $\propto Z^4$ ) and line radiation. Evidence of heterogeneous hot spot mix is observed experimentally through spectrally resolved measurements<sup>11</sup> and broadband ( $> 8\text{ keV}$ ) gated x-ray images. In the latter hot spot mix manifests as bright spots, providing evidence of some heterogeneous mixing of ablator material [glow-discharge-polymer (GDP, CH<sub>1.3</sub>O<sub>0.02</sub>), germanium (Ge) doped GDP, or silicon (Si) doped GDP] with the lower Z hot spot.

In this study Fourier analysis is used to identify the intensity of large-scale characteristics of the implosion, describing size and shape, and the small-scale features, corresponding to the bright spots, spatially resolving regions of high-mix. The bright spot

features are tracked in  $x$ - and  $k$ - space, enabling identification of predominant seeding features and origin of capsule material entering the hot spot.

The experimental configuration is described in Section II. Section III describes image processing in Fourier space and error analysis. Results are presented in Section IV, and conclusions are presented in Section V.

## II. EXPERIMENTAL CONFIGURATION

Imploding targets are imaged along the hohlraum symmetry axis onto one of two time-resolved, x-ray diagnostics: a gated x-ray detector (GXD)<sup>12,13</sup> or a hardened gated x-ray imager (HGXI)<sup>14</sup>. An imaging snout containing filters and pinhole arrays is attached to the front of the x-ray framing camera.<sup>12,13</sup> The pinhole array contains over one hundred closely packed 10  $\mu\text{m}$  diameter pinholes, designed to assure at least one row of pinholes is fully imaged on a given strip on the microchannel plate. When nominal alignment is achieved, three pinhole rows are fully imaged, providing duplicate images in time. The pinhole array is located 10 cm from target chamber center (TCC) yielding a  $\sim 12\times$  magnification of the imploding target on the detector plane,  $\sim 1.3$  m from TCC.

Gated images are collected on four strips of the x-ray framing camera with typical interstrip gate timings of 200-, 400-, and 600-ps relative to the first strip, resulting in a total time window close to 1 ns. GXD images are recorded using CCD readout. The HGXI is designed to operate on implosions with neutron yields up to  $\sim 10^{15}$ , recording images on film so that neutron background does not affect data quality.<sup>15</sup> GXD and HGXI have a recording spatial resolution of 9 and 20  $\mu\text{m}/\text{px}$  respectively, translating to  $\sim 0.7$  and  $\sim 1.6$   $\mu\text{m}/\text{px}$  on the target plane. The system resolution with imaging snout

(GXD or HGXI) is limited by the geometrical resolution set by the nominal pinhole size of 10  $\mu\text{m}$ . Both these diagnostics are flat-fielded for spatial variations in photosensitivity across the strip of the x-ray framing camera and are absolutely timed relative to the NIF laser with dedicated timing shots at NIF.<sup>8,12–14</sup>

Pinhole image frames are extracted from the full-aperture camera image after detector response corrections by projecting the known pinhole pattern onto the detector plane. Small variations in the magnification and translations in x- and y-axes are applied to match the projected pattern to the observed images, accounting for deviation in snout pointing and pinhole array location from nominal insertion depth. The resulting images correspond to broadband x-ray measurements with  $h\nu > 8 \text{ keV}$ , filtering low energy x-rays with 2.5 mm of Kapton. Individual frames are integrated over  $\sim 40$  or  $100 \text{ ps}$  (depending on the instrument and voltage settings), and are nominally spaced  $\sim 20\text{--}25 \text{ ps}$  apart.<sup>16</sup>

### III. IMAGE PROCESSING FOR BRIGHT SPOT ANALYSIS

The power spectrum density (PSD) describes the average signal power at a given frequency. In this study it represents the sum of the squares of the Fourier amplitudes, describing the frequency or wavenumber distribution of the intensity modulations in the gated x-ray implosion images. The PSD is used to quantify the average amount of detectable features of a given scale size. Here the PSD,  $G(k)$ , is calculated as<sup>17</sup>

$$G(k_n) = \sum_{\sqrt{m^2+l^2}=v_n} |F(m,l)|^2, \quad (1)$$

where  $F(m,l)$  is the 2D Fourier transform described as

$$F(m,l)=\frac{1}{N^2}\sum_{m=0}^{N-1}\sum_{l=0}^{N-1}f(i,j)e^{\frac{12\pi}{N}(im+lj)} \quad . \quad (2)$$

Here  $f(i,j)$  is the indexed  $N \times N$  input image. Simulated data was used to investigate the effects on the PSD when introducing bright spots. Simulated images are shown in Figure 2 (a)-(c) and their corresponding PSD is displayed in Figure 2 (d). Figure 2 (a) shows a data simulated frame, represented by a Gaussian with FWHM of 80  $\mu\text{m}$ . Its PSD closely resembles the envelope intensity distribution of the hot spots under consideration, where no high wavenumber contributions are present. Superimposing a Gaussian feature with FWHM of 30  $\mu\text{m}$ , [see Figure 2 (b)] causes an observable change in the PSD, where now high wavenumber contributions are observed. In Figure 2 (c) the FWHM of the bright spot is decreased to 12  $\mu\text{m}$  and its relative brightness is increased by a factor of five. The PSD is sensitive to both these changes, observing a broadened distribution toward higher wavenumbers, with higher power density values. Note that superimposing a bright spot onto a smooth Gaussian hot spot results in a broadband PSD. Because the PSD is sensitive to the frequency distribution of the intensity modulations, one can identify the emergence of bright spots and clearly distinguish between a homogenous mix, having only low wavenumber envelope structure, and heterogeneous mix of ablator in the hot spot, having both low wavenumber envelope structure and high wavenumber bright spot features leading to a broadband spectrum. The 17% contour is often used to describe the capsule symmetry; it is shown as reference for all images.

Fourier analysis was used to discriminate between the low wavenumber intensity envelope of the hot spot and the high wavenumber bright spot features in x-ray gated images. The image envelope was determined by applying a high-order ( $n=6$ ) super Gaussian low pass filter in Fourier space. Due to the higher convergence of the cryogenic



DT layered target implosions compared to the Symcap implosions, a low pass filter with  $k < 0.105 \mu\text{m}^{-1}$  and  $k < 0.160 \mu\text{m}^{-1}$  were used for Symcap and the cryogenic DT layered targets, respectively. These filters were empirically determined based on the PSD of various experimental images. The 17% contour of the low pass filtered image was used as a metric to establish an accurate description of the implosion shape. For layered targets a higher low pass filter cutoff was necessary in order to accurately represent the implosion shape. This is mainly because the emitting volume is smaller for layered targets due to higher convergence, requiring higher wavenumbers to adequately describe their shape. Image bright spots were identified by applying a high-order ( $n=20$ ) super Gaussian notch filter in Fourier space bounded by the envelope cutoff and the instrument resolution element ( $0.105 \mu\text{m}^{-1} < k < 0.63 \mu\text{m}^{-1}$  for Symcap targets, and  $0.160 \mu\text{m}^{-1} < k < 0.63 \mu\text{m}^{-1}$  for layered targets).

Figure 3 demonstrates the results of such image filtering on Symcap shot N110208 at time 21.34 ns, corresponding to a Ge-doped target ablator. The input raw gated x-ray image, viewed from the pole, is shown in Figure 3 (a) where the red line indicates the fill tube location,  $232^\circ$  in this case, and the white lines provide reference to  $\phi=0^\circ$  and  $78^\circ$  lines of sight in target chamber coordinates. The boundary of the hot spot is defined as the intensity contour in the gated x-ray image that is 17% of the peak intensity. The envelope image, shown in Figure 3 (b), is used to determine the 17% contour. Overlaying this contour onto the raw image, shown as the white curve in Figure 3 (a), shows the 17% contour based on the image envelope adequately describes the implosion shape, validating the low pass filter choice. The curves and line markers described for the input image are likewise included for the envelope and bright spot images. Isolated bright

spots, identified by the filter described above, are captured in Figure 3 (c) close to the vicinity of the fill tube. Features significantly dimmer than the bright spots, as those observed outside the 17% contour, are attributed to noise in the imaging diagnostic, which has a broadband spectrum in wavenumber.

The normalized PSD of the input raw image as a function of wavenumber ( $\mu\text{m}^{-1}$ ) is shown in Figure 3 (d) as the solid magenta curve, along with dotted red and dashed green curves depicting the low-pass and notch filters. Figure 3 (e) shows the PSD corresponding to the low-pass filtered image, solid red, and notch filtered image, shaded green. The black dashed vertical line marks the cutoff wave number set by the instrument resolution, and the instrument contribution to the PSD is shown as the shaded region in Fig. 3 (e) and (d). The inherent PSD noise level due to the instrument was determined by using flat field shots where a gold-coated GDP sphere is directly irradiated by the laser using a  $\sim 2\text{-}3$  ns square pulse, to generate a uniform x-ray irradiation onto the detector. Various frames were chosen and their PSD was calculated, showing statistical variation between them. The shaded region shown in Fig. 3 (e) and (d) represents the average PSD noise. This analysis showed the HGXI has a higher PSD noise in comparison to GXD, likely due to film noise.

Hydrodynamic simulations have shown target defects can seed perturbations that can transport ablator material into the hot spot.<sup>5</sup> The target fill tube is an obvious isolated target perturbation acting as a seed for the ablation front hydrodynamic instability. To investigate the fill tube contribution to the generation of bright spots, the filtered bright spot images were binned azimuthally in order to correlate bright spot intensity and fill tube location. The filtered bright spot image signal was integrated in  $5^\circ$  bins within the

17% contour and normalized to the total image signal of the raw input image within the 17% contour. HGXI and GXD are not absolutely calibrated, thus x-ray emission measured with these diagnostics is only a relative measurement. Normalizing the integrated signal in the bright spots with the x-ray emission measured by the raw input image enables comparison between shots. The normalized integrated values represent the emission fraction contributed by bright spots in a given  $5^\circ$  area to the total integrated implosion emission.

Figure 4 shows the normalized bright spot emission as a function of  $\phi$  for Symcap shot N110208 at 21.34 ns. The fill tube location (at  $232^\circ$ ) and  $180^\circ$  from the fill tube are marked by red dashed lines. The inset shows the filtered bright spot image [Figure 3 (c)], depicting one  $5^\circ$  integration region shaded in white. For this frame the analysis shows a strong correlation between bright spots and the fill tube location, with two prominent peaks close to the fill tube location, between  $220^\circ$  and  $250^\circ$ . This analysis was applied to all data frames for shot N110208. By time integrating the normalized bright spot emission for each  $\phi$  position, using all available frames, bright spot location information can be collapsed onto a single plane as shown in Figure 5. This figure shows there is a strong correlation between observed bright spots and fill tube location for the Symcap implosion (shot N110208).

#### **IV. RESULTS AND DISCUSSION**

Experiments geared toward the National Ignition Campaign at NIF were ongoing between 2009 to 2012. Results presented here pertain to a subset of experiments between 2010-2011, amounting to a total of 23 shots that include Symcap (thirteen shots, where

five were convergent ablator experiments- conA<sup>18</sup>), DT (six shots), and THD (four shots) experiments. Frames for all shots were analyzed as described in Sec. III.

### A. Filtered images and PSD

The PSD is calculated for every frame registering a complete imploding capsule image (i.e. frames with clipped images are ignored) for all 23 shots. The number of available frames varies for each shot and is dependent on the framing camera timing relative to peak x-ray emission – bang time ( $t_b$ ). As a consequence the number of available images before and after  $t_b$  varies between shots. All measured PSD display a high- broadband spectrum indicating a heterogeneous mixture of ablator material in the hot spot plasma, which varies as a function of time. The PSD for Symcap shots displays little variation in the wavenumber ( $k$ ) distribution below  $0.1 \mu\text{m}^{-1}$ ; changes in the spectrum are observed mainly between  $0.1$ - $0.63 \mu\text{m}^{-1}$  as a function of time. This means the envelope or overall shape for Symcaps varies little as a function of time, and temporal changes are mostly due to bright spot evolution. Such is not the case for cryogenic DT layered targets, which display variations in the distribution in both these regimes, though showing more pronounced changes between  $0.16$ - $0.63 \mu\text{m}^{-1}$  as the implosion progresses.

The normalized PSD begins to decrease at  $k = 0.07 \mu\text{m}^{-1}$  for Symcap shots, exhibiting a sharp drop in the frequency distribution between  $0.1$  to  $0.15$ - $0.2 \mu\text{m}^{-1}$  which does not increase significantly for higher wavenumbers. The normalized power/ $\mu\text{m}^{-1}$  at the cutoff wavenumber for Ge-ablator Symcaps is close to 10 times higher than that of Si-ablator Symcaps. In the case for DT experiments, a decrease in the normalized PSD is subtly observed at  $k > 0.07 \mu\text{m}^{-1}$ . In most cases no distinct drop is observed in the frequency

distribution of these experiments, as observed for Symcaps, but rather a slight decline with higher wavenumber is observed reaching typical normalized power/ $\mu\text{m}^{-1}$  values of 0.007-0.1 at the cutoff wavenumber for shots with both Ge and Si ablators. The observed differences in the normalized PSD between Symcap and layered shots, described above, are consistent with the higher convergence of DT and THD experiments requiring higher power density for wavenumbers above the Symcap drop-off to describe their large scale structure.

Figure 6 shows a matrix of normalized PSD results for Symcap and DT experiments with Ge and Si ablators at  $t_b$ . The normalized PSD is shown as the solid blue line, and the envelope and bright spot contribution are shown as the red line and shaded green region. The dashed gray line and gray shaded region denote the cut-off wavenumber and instrument normalized PSD noise level. In addition to the differences mentioned previously, we see DT shots have slightly higher power density at  $k > 0.2 \mu\text{m}^{-1}$  in comparison to Symcap shots. This indicates DT heterogeneous hot spot mix has brighter emission relative to the hot spot plasma in comparison to Symcaps. At  $k = 0.15 \mu\text{m}^{-1}$  ( $\sim 40 \mu\text{m}$  scale) the bright spot contribution to the normalized PSD varies on average by a factor of two between Ge- and Si-doped ablator targets, with higher values corresponding to Ge-doped targets. The ratio between the bright spot contribution to the PSD for Ge- and Si-doped Symcap targets follows an increasing trend for higher wavenumbers; for  $k = 0.3, 0.4,$  and  $0.5 \mu\text{m}^{-1}$  values for Ge-doped targets are larger, on average, by factors of 5, 6, and 10. For layered targets the ratio between normalized bright spot PSD for Ge- and Si-doped targets is mostly steady, fluctuating between ratios of 0.8 to 3 for  $k \geq 0.3 \mu\text{m}^{-1}$ . The bright spot contribution to the normalized PSD shows Ge- and Si-doped capsules

exhibit considerably different results for Symcap targets, while little change is observed for DT targets using different ablator dopants. This can be an indication that hot spot mix for Symcap and layered capsules corresponds to different capsule layers; Symcap hot spot mix composed mostly of doped ablator material, layered capsule hot spot mix composed mostly of clean GDP or ice.

Bright spot behavior is also portrayed in  $x$ - and  $y$ -space. Figure 7 shows the result of normalizing the bright spot image by the envelope image, indicating modulations relative to the envelope (see color bar units). Frames for each shot correspond to time  $\sim(t_b-100\text{ps})$ ,  $t_b$ , and  $\sim(t_b+100\text{ps})$  depending on frame time availability. The trajectory of each bright spot is view dependent. Though this represents a small subset of images and shots, one can appreciate the wide palette of bright spots that are observed; some travel toward the center of the target as it implodes (N110208), others remain quasi-static in time (bright spot near fill tube for N110608), and some become brighter as the implosion progresses (N100929). Regardless of their spatio-temporal behavior comparison between shot frames shown in Figure 7, a Symcap, DT, and THD, all with Ge-doped ablator, shows layered targets' bright spot emission is at or above the local envelope value, while for Symcap shots bright spot emission is around half that of the envelope. These trends are consistent throughout other Ge-ablator shots. It should be noted that for targets with a Si ablator bright spots were also identified; for Symcaps their brightness relative to the envelope was on average lower than their Ge counterparts, for layered targets brightness values were comparable to those with Ge, consistent with normalized PSD results.

## **B. Fill tube correlation**

As described in Section II, a time-integrated plot describing the bright spot spatial distribution as a function of  $\varphi$  (azimuthal angle in degrees) was calculated for each shot in order to identify any correspondence between bright spot and fill tube location. To compile all measured results, all data is collapsed into a single plot sorted by type of shot (Symcap vs. layered). Time integrated results for each shot type were averaged, highlighting the dominant trends. Figure 8 (a) and (b) show results for Symcap and layered shots respectively. On average the fill tube is a dominant seed for Symcap shots, corresponding to the broadest and brightest bright spot emission feature as a function of  $\varphi$ , though offset  $\sim 30^\circ$  from the fill tube location. This offset could be due to the generation of a material jet at an offset angle or a translation in the fill tube location as the capsule implodes. For layered targets a broad peak centered around  $40^\circ$  from the fill tube and spanning close to  $50^\circ$  is observed. The brightest features, however, are observed around  $90^\circ$  from the fill tube. This analysis shows the fill tube is a seeding source generating hot spot mix in both Symcap and layered implosions. For symcaps the fill tube is the largest contributor to mix, while for layered targets other seeding sources have higher contributions.

### C. Bright spot power

Integration of the PSD yields the total power corresponding to an image. The total PSD and the bright spot contribution to the total PSD were used to determine the fractional power corresponding to bright spots. Figure 9 shows the fractional power measured for all shots at peak x-ray emission ( $t_b$ ), with Symcap, DT, and THD shots shown as the green, red, and dark red diamonds, respectively. Here shots with Si ablator

are circled with an orange solid line. Due to the pinhole array pattern projected onto the x-ray imager, there are cases where two images are recorded at the same position in time along a strip. These temporal duplicate images were used to determine the error in the PSD by comparing the PSD between the images and calculating the fractional difference between the two frames. All available duplicate frames were analyzed, yielding errors in fractional power of  $\sim 10\%$ .

For this series of shots, a large variance in fractional bright spot power at  $t_b$  is observed for Symcap shots ranging over 0.01-0.10. For cryogenic DT-layered targets the variation is between 0.04-0.11. This plot corroborates previous observations showing the bright spot power is slightly higher for layered targets in comparison to sycamp targets. If we compare experiments with similar conditions (laser pulse, hohlraum, laser energy, etc), we see there is a distinct difference between Ge and Si ablator bright spot fractional power for Symcap capsules. Shots N110625, N110627, and N110630 belong to a particular Symcap campaign; here N110625 and N110627 used the same hohlraum design, gas fill, and laser pulse shape, differing only on ablator dopant: Ge for N110625 and Si for N110627. N110630 used a Si ablator, with the laser main drive pulse extended by 230 ps in comparison to that used for N110625 and N110627. The observed fractional bright spot power for both N110627 and N110630 is close to 0.04, significantly lower than N110625 having fractional bright spot power just above 0.1. Shots N110821 (Si), N110731 (Si), and N110807 (Ge) belong to another Symcap campaign; here too Si ablator shots have lower fractional power than their Ge counterparts. If the majority of mix material entering the hot spot originates from the doped GDP layer only, then qualitatively one would expect this type of behavior due to differences in atomic number



between Ge and Si. Figure 9 shows that such qualitative difference is not observed for cryogenic DT layered shots. If most of the material mixing into the hot spot originates from the doped GDP layer, then observing changes in fractional bright spot power among capsules with different Z dopants is expected, as shown for Symcap capsules analyzed in this study. Not observing the same behavior for DT and THD capsules suggests that the un-doped ablator layers dominate the mix entering the hot spot. This would imply the material composition of hot spot mix differs among Symcap and layered capsules.

In addition to diagnosing broadband x-ray emission as a function of time using framing cameras, time-integrated spectrally-binned images are also recorded on an image plate, referred to as Ross filter images.<sup>19,20</sup> These images use the same pinhole array as the framing camera but are detected on an image plate detector surrounding the active area of the x-ray framing camera. These filters are matched in material and thickness such that differences in transmission for given pairs yields spectral bandwidths integrating spectral data over  $\sim 3\text{-}9$  keV ranges; these bandwidths have centroids between 6-18 keV. A subset of Ross pair images were analyzed using the same methodology applied to framing camera images. Results obtained are consistent with framing camera observations, where bright spot fractional power showed no difference between layered (DT/THD) Si and Ge capsules, but lower fractional power was observed for Si doped Symcap capsules in comparison to Ge doped Symcap capsules. The latter suggests mix mass entering layered targets is not predominantly originating from the doped layer (Ge or Si). In this case mix could be attributed to the clean GDP layer or DT ice injected into the hot spot. Spectrally resolved measurements were used to test this hypothesis.

For a number of experiments the hot spot x-ray spectrometer (HSXRS)<sup>11</sup> was simultaneously run. The HSXRS is an absolutely calibrated PET crystal spectrometer recording time-integrated 1D spectral images between 9.75 to 13.1 keV, designed to measure Ge k-shell emission. The measured Ge He $_{\alpha}$  line and satellite emission is used to determine the amount of Ge hot spot mix mass for implosions.<sup>11</sup>

The strength of the Ge He $_{\alpha}$  line and its associated satellite emission (J/sr) as observed by the HSXRS is compared to the fractional power attributed to bright spots for Ge ablator shots. Results for Symcaps are shown in Figure 10 (a) where an increasing trend is observed showing a positive correlation between hot spot mix mass and bright spot power as determined by the filtered images. Figure 10 (b) shows the same comparison for the layered shots. Here the Ge He $_{\alpha}$  line and satellite emission remains fairly constant regardless of increasing bright spot power. Spectral data from the HSXRS corroborates the hypothesis that bright spots evident in Symcap x-ray gated images mostly correspond to material originating from the doped GDP layer, while such is not the case for layered targets.

Hydrodynamics simulations investigating mix observe a larger contrast between bright spots and their surrounding material at times  $\sim 100$  ps before  $t_b$ .<sup>21</sup> The fractional power was evaluated 100 ps before  $t_b$ , however larger contrast was not consistently observed; over half of the shots showed lower or close to equal fractional power. For those experiments that did show higher bright spot contrast at 100 ps before bang time, an increase in contrast was observed anywhere between 20-40%.

Results described above correspond to a subset of experiments available at the time this study began. Future work will include more recent experiments, and

will also include analysis of broadband x-ray images viewing the implosion through a window at the hohlraum/capsule equator. Utilizing two views having perpendicular lines of sight may aid in more accurately describing bright spot trajectory and size. Capsules fielded at NIF go through a stringent metrology process where not only capsules layers are characterized, but also surface roughness and defects (mounds, indentations, scratches, etc.) are documented. The next phase of this study will aim to correlate measured bright spots with known target defects.

## V. CONCLUSIONS

Fourier analysis of gated x-ray images was used to filter bright spot features observed inside the implosion hot spot, spatially resolving the growth and development of high-mix features. Their temporal behavior was characterized in both  $x$ - and  $k$ -space, emphasizing differences between Symcap and cryogenic DT/THD layered target implosion shots. The PSD, calculated for all image frames, shows structure characteristic of heterogeneous mixing composed of large-scale structure features described by the image envelope, and small-scale structure corresponding to bright spots emission. Both the PSD and fractional bright spot power show layered targets (DT/THD) have higher bright spot power contributions compared to Symcaps, with no distinct differences between shots with Ge- or Si- ablators. Symcap shots, however, show bright spot power variances between Ge- and Si-ablator capsules, where less power/emission was measured for Si targets. These results suggest most material entering the hot spot originates from different ablator layers for Symcap and layered shots; most of the mix mass corresponds

to doped GDP (Ge or Si) for the first case, while for the second case, material likely originates from the clean GDP layer since fractional bright spot power levels are comparable for both doped ablator materials. Bright spot power results were correlated with spectroscopic measurements from the HSXRS and Ross filter images, supporting the above hypothesis.

For all image frames, the bright spot emission was mapped as a function of azimuthal angle to investigate correspondence between bright spot and fill tube location. After time integration within shots, and averaging these results within types of shots, it is clear the fill tube is a seeding mechanism for the generation of bright spots in both Symcap and layered (DT/THD) targets. For Symcaps this amounts to the most predominant perturbation as a function of azimuthal angle, while for layered targets we observe features with comparable emission levels at other locations away from the fill tube.

## **ACKNOWLEDGMENT**

The authors acknowledge the members of the NIF operations team for their efforts in supporting these experiments. This work was performed at LLNL under the auspices of the U.S. Department of Energy under contract DE-AC52-07NA27344.

## FIGURE CAPTIONS

FIG. 1. (Color online) Cross-section of capsule used for NIF experiments, with GDP ablator doped with various levels (0 %, 0.2%, 0.5%) of Ge (orange layers). For layered targets the capsule ablator surrounds a layer of DT (or THD) ice (dark blue) that in turn confines the DT (THD) gas (light blue). For symmetry capsules (Symcaps) the ice layer is replaced with a mass equivalent layer of GDP, and the GDP shell is filled with a mixture of He and D<sub>2</sub> gas. Some capsules replace Ge dopant with various levels of Si dopant.

FIG. 2. (Color online) Simulated x-ray image of the implosion near stagnation for the following: (a) a Gaussian intensity profile signal with FWHM of 80  $\mu\text{m}$  describing a homogenous mix of material. (b) Simulated image as described in (a) with superimposed off-center bright spot with 30  $\mu\text{m}$  FWHM. (c) Simulated image as described in (a) with superimposed off-center bright spot with 12  $\mu\text{m}$  FWHM with  $\sim 5\text{X}$  higher emission. (d) Normalized power spectra density (PSD) as a function of wavenumber, for images in (a) (blue curve), (b) (red curve) and (c) (green curve). PSD for simulated image for homogenous case, (a), shows no structure for wavenumbers larger than  $\sim 0.12 \mu\text{m}^{-1}$ . Superposition of bright spot translates to a change in PSD, having structure above  $\sim 0.12 \mu\text{m}^{-1}$ . Superposition of a smaller bright spot (FWHM 12  $\mu\text{m}$ ) with higher emission ( $\sim 5\text{X}$ ) is also tracked via the PSD, where

the spectral distribution extends over  $\sim 0.5 \mu\text{m}^{-1}$  and normalized power spectral density is higher than in either of the previous cases.

FIG. 3. (Color online) Compilation of input and Fourier filtered images, with corresponding PSD for a Symcap capsule. The raw image input, spatial intensity envelope of the hot spot, and the bright spot images are shown in (a), (b), and (c), with white line markers depicting  $\varphi = 0^\circ$  and  $78^\circ$ , and red marker showing fill tube location. The white curve around the implosion is the 17% of peak intensity contour determined from the envelope image, validating the use of the envelope as an adequate description of large-scale structure/shape of the implosion. Image (c) highlights the use of Fourier filtering to identify emission features with spatial structure between  $\sim 10$  and  $50 \mu\text{m}$ . Note that bright spots that are difficult to identify on the input image (a) are evident on the bright spot image (c). The low emission structure seen in (c) is related to the broadband instrument noise. (d) Calculated PSD for input image is shown as solid blue curve and super-Gaussian filters (dotted red curve for low pass filter, and dotted green for notch filter used for bright spot analysis). A cutoff- wavenumber, determined by the resolution element of the diagnostics, is shown as the dashed black line in (d) and (e); it sets the wavenumber upper bound for the notch filter applied to the input image. (e) The normalized PSD for the input image described in (d) is compared with the PSD contributions from the envelope and bright spot images, shown as the solid red curve and shaded green region. The gray shaded region denotes the diagnostic noise level.

FIG. 4. (Color online) Bright spot emission for Symcap shot N110208 (integrated over of  $5^\circ$  azimuthal bins as shown in inset) within the 17% contour (normalized to total emission per input image) as a function of  $\varphi$  at  $t=21.34$  ns. Dashed vertical red lines indicate fill tube (FT) location and  $180^\circ$  from FT. In this frame a strong correlation between bright spot- and fill tube- location is clearly identified.

FIG. 5. (Color online) Time integrated (normalized) bright spot emission using all the available image frames recorded throughout the implosion for shot N110208 (Symcap), show a large portion of bright spots are generated close to the fill tube location. Dashed red lines indicate fill tube (FT) location and  $180^\circ$  from FT.

FIG. 6. (Color online) Normalized PSD (solid blue curve) and contributions to the PSD from envelope (solid red curve) and bright spots (shaded green), for four different types of implosions. Graphs on the left (right) column show Symcap (DT) shots with Ge- and Si- doped GDP ablator at peak x-ray emission. Dashed gray line and shaded gray region denote cut-off wavenumber and instrument noise respectively. Normalized PSD shows DT experiments have higher power for  $k > 0.2 \mu\text{m}^{-1}$  compared to Symcaps. Symcap targets with Si doped GDP ablator show lower bright spot contribution to the normalized PSD in comparison to Ge doped ablator targets for  $k > 0.1$ . Differences in bright spot contribution to the normalized PSD between Ge- and Si- doped ablator DT implosion are not as pronounced at those observed in Symcap experiments.

FIG. 7. (Color online) Bright spot filtered images normalized by the local envelope values, showing modulations above the envelope for a compilation of Ge- doped ablator targets (from left to right: Symcap, DT, and THD). Middle frame corresponds to peak x-ray emission, top and bottom frames are  $\sim 100$  ps before and after peak x-ray emission; image markers as described in previous figures. Filtered images show Symcap bright spots have modulations below the intensity envelope of the hot spot, while layered targets (DT/THD) have bright spots at or above the intensity envelope emission level. This small subset of frames shows bright evolution behavior varies among shots.

FIG. 8. (Color online) Time integrated average bright spot emission (normalized to total input image emission within 17% contour) as a function of degrees from fill tube, for Symcap (a) and layered (b) targets. Data shows the fill tube seeds bright spots for both Symcap and DT/THD shots. This feature is most predominant for Symcap experiments. For layered shots, however, comparable features are also measured away from the fill tube.

FIG. 9. (Color online) Power contribution from bright spots normalized by total power from raw input image PSD (fractional power) for all analyzed shots at peak x-ray time. Results for Symcap, DT, and THD are shown as the green, red, and dark red diamonds, respectively. Shots with Si-doped GDP ablator are denoted by orange circle. Note fractional power levels differ between different ablator shots for Symcaps, though remain stable for cryogenic DT layered shots.



FIG. 10. (Color online) Comparison between Ge He $_{\alpha}$  line and satellite emission (J/sr) measured by the HSXRS, with bright spot fractional power results for (a) Symcap and (b) DT and THD targets. Spectroscopy measurements suggest higher Ge mix mass can be correlated with higher values of fractional bright spot power for the Symcap implosions, but this trend is not observed for layered targets, where Ge emission values remain moderately constant with increasing bright spot fractional power.

## REFERENCES

- <sup>1</sup> G.H. Miller, E.I. Moses, and C.R. Wuest, *Opt. Eng.* **443**, (2004).
- <sup>2</sup> G.H. Miller, E.I. Moses, and C.R. Wuest, *Nuclear Fusion* **44**, (2004).
- <sup>3</sup> S.W. Haan, J.D. Lindl, D.A. Callahan, D.S. Clark, J.D. Salmonson, B.A. Hammel, L.J. Atherton, R.C. Cook, M.J. Edwards, S. Glenzer, A.V. Hamza, S.P. Hatchett, M.C. Herrmann, D.E. Hinkel, D.D. Ho, H. Huang, O.S. Jones, J. Kline, G. Kyrala, O.L. Landen, B.J. MacGowan, M.M. Marinak, D.D. Meyerhofer, J.L. Milovich, K.A. Moreno, E.I. Moses, D.H. Munro, A. Nikroo, R.E. Olson, K. Peterson, S.M. Pollaine, J.E. Ralph, H.F. Robey, B.K. Spears, P.T. Springer, L.J. Suter, C.A. Thomas, R.P. Town, R. Vesey, S.V. Weber, H.L. Wilkens, and D.C. Wilson, *Physics of Plasmas* **18**, 051001 (2011).
- <sup>4</sup> B.A. Hammel, H.A. Scott, S.P. Regan, C. Cerjan, D.S. Clark, M.J. Edwards, R. Epstein, S.H. Glenzer, S.W. Haan, N. Izumi, J.A. Koch, G.A. Kyrala, O.L. Landen, S.H. Langer, K. Peterson, V.A. Smalyuk, L.J. Suter, and D.C. Wilson, *Physics of Plasmas* **18**, 056310 (2011).
- <sup>5</sup> B.A. Hammel, S.W. Haan, D.S. Clark, M.J. Edwards, S.H. Langer, M.M. Marinak, M.V. Patel, J.D. Salmonson, and H.A. Scott, *High Energy Density Physics* **6**, 171 (2010).

<sup>6</sup> T.R. Boehly, V.N. Goncharov, W. Seka, M.A. Barrios, P.M. Celliers, D.G. Hicks, G.W. Collins, S.X. Hu, J.A. Marozas, and D.D. Meyerhofer, Phys. Rev. Lett. **106**, 195005 (2011).

<sup>7</sup> H.F. Robey, T.R. Boehly, P.M. Celliers, J.H. Eggert, D. Hicks, R.F. Smith, R. Collins, M.W. Bowers, K.G. Krauter, P.S. Datte, D.H. Munro, J.L. Milovich, O.S. Jones, P.A. Michel, C.A. Thomas, R.E. Olson, S. Pollaine, R.P.J. Town, S. Haan, D. Callahan, D. Clark, J. Edwards, J.L. Kline, S. Dixit, M.B. Schneider, E.L. Dewald, K. Widmann, J.D. Moody, T. Döppner, H.B. Radousky, A. Throop, D. Kalantar, P. DiNicola, A. Nikroo, J.J. Kroll, A.V. Hamza, J.B. Horner, S.D. Bhandarkar, E. Dzenitis, E. Alger, E. Giraldez, C. Castro, K. Moreno, C. Haynam, K.N. LaFortune, C. Widmayer, M. Shaw, K. Jancaitis, T. Parham, D.M. Holunga, C.F. Walters, B. Haid, E.R. Mapoles, J. Sater, C.R. Gibson, T. Malsbury, J. Fair, D. Trummer, K.R. Coffee, B. Burr, L.V. Berzins, C. Choate, S.J. Brereton, S. Azevedo, H. Chandrasekaran, D.C. Eder, N.D. Masters, A.C. Fisher, P.A. Sterne, B.K. Young, O.L. Landen, B.M. Van Wonterghem, B.J. MacGowan, J. Atherton, J.D. Lindl, D.D. Meyerhofer, and E. Moses, Physics of Plasmas **19**, 042706 (2012).

<sup>8</sup> J.D. Lindl, *Inertial Confinement Fusion: The Quest for Ignition and Energy Gain Using Indirect Drive* (Springer-Verlag, 1998).

<sup>9</sup> E.S. Dodd, J.F. Benage, G.A. Kyrala, D.C. Wilson, F.J. Wysocki, W. Seka, V.Y. Glebov, C. Stoeckl, and J.A. Frenje, Physics of Plasmas **19**, 042703 (2012).

<sup>10</sup> G.A. Kyrala, D.C. Wilson, J.F. Benage, M. Gunderson, K. Klare, J. Frenje, R. Petrasso, W. Garbett, S. James, V. Glebov, and B. Yaakobi, High Energy Density Physics **3**, 163 (2007).

<sup>11</sup> S.P. Regan, R. Epstein, B.A. Hammel, L.J. Suter, J. Ralph, H. Scott, M.A. Barrios, D.K. Bradley, D.A. Callahan, C. Cerjan, G.W. Collins, S.N. Dixit, T. Doeppner, M.J. Edwards, D.R. Farley, S. Glenn, S.H. Glenzer, I.E. Golovkin, S.W. Haan, A. Hamza, D.G. Hicks, N. Izumi, J.D. Kilkenny, J.L. Kline, G.A. Kyrala, O.L. Landen, T. Ma, J.J. MacFarlane, R.C. Mancini, R.L. McCrory, N.B. Meezan, D.D. Meyerhofer, A. Nikroo, K.J. Peterson, T.C. Sangster, P. Springer, and R.P.J. Town, Physics of Plasmas **19**, 056307 (2012).

<sup>12</sup> J.A. Oertel, R. Aragonez, T. Archuleta, C. Barnes, L. Casper, V. Fatherley, T. Heinrichs, R. King, D. Landers, F. Lopez, P. Sanchez, G. Sandoval, L. Schrank, P. Walsh,

P. Bell, M. Brown, R. Costa, J. Holder, S. Montelongo, and N. Pederson, Review of Scientific Instruments **77**, 10E308 (2006).

<sup>13</sup> G.A. Kyrala, S. Dixit, S. Glenzer, D. Kalantar, D. Bradley, N. Izumi, N. Meezan, O.L. Landen, D. Callahan, S.V. Weber, J.P. Holder, S. Glenn, M.J. Edwards, P. Bell, J. Kimbrough, J. Koch, R. Prasad, L. Suter, J.L. Kline, and J. Kilkenny, Review of Scientific Instruments **81**, 10E316 (2010).

<sup>14</sup> S. Glenn, J. Koch, D.K. Bradley, N. Izumi, P. Bell, J. Holder, G. Stone, R. Prasad, A. MacKinnon, P. Springer, O.L. Landen, and G. Kyrala, Review of Scientific Instruments **81**, 10E539 (2010).

<sup>15</sup> N. Izumi, C. Hagmann, G. Stone, D. Hey, S. Glenn, A. Conder, A. Teruya, C. Sorce, R. Tommasini, W. Stoeffl, P. Springer, O.L. Landen, H.W. Herrmann, G.A. Kyrala, R. Bahukutumbi, V.Y. Glebov, T.C. Sangster, M. Eckart, A.J. Mackinnon, J.A. Koch, D.K. Bradley, and P. Bell, Review of Scientific Instruments **81**, 10E515 (2010).

<sup>16</sup> S. Glenn and L.R. Benedetti, *Private Communication* (2011).

<sup>17</sup> R.M. Howard, *Principles of Random Signal Analysis and Low Noise Design: The Power Spectral Density and Its Applications* (John Wiley & Sons, Inc., 2002).

<sup>18</sup> D.G. Hicks, N.B. Meezan, E.L. Dewald, A.J. Mackinnon, R.E. Olson, D.A. Callahan, T. Döppner, L.R. Benedetti, D.K. Bradley, P.M. Celliers, D.S. Clark, P. Di Nicola, S.N. Dixit, E.G. Dzenitis, J.E. Eggert, D.R. Farley, J.A. Frenje, S.M. Glenn, S.H. Glenzer, A.V. Hamza, R.F. Heeter, J.P. Holder, N. Izumi, D.H. Kalantar, S.F. Khan, J.L. Kline, J.J. Kroll, G.A. Kyrala, T. Ma, A.G. MacPhee, J.M. McNaney, J.D. Moody, M.J. Moran, B.R. Nathan, A. Nikroo, Y.P. Opachich, R.D. Petrasso, R.R. Prasad, J.E. Ralph, H.F. Robey, H.G. Rinderknecht, J.R. Rygg, J.D. Salmonson, M.B. Schneider, N. Simanovskaia, B.K. Spears, R. Tommasini, K. Widmann, A.B. Zylstra, G.W. Collins, O.L. Landen, J.D. Kilkenny, W.W. Hsing, B.J. MacGowan, L.J. Atherton, and M.J. Edwards, Physics of Plasmas **19**, 122702 (2012).

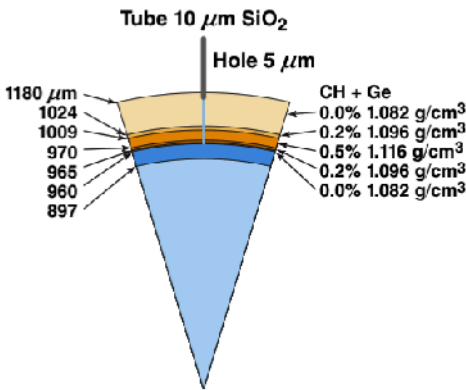
<sup>19</sup> H.A. Compton and S.K. Allison, *X-ray in Theory and Experiment* (D.Van Nostrand Compary, Inc., New Jersey, 1963).

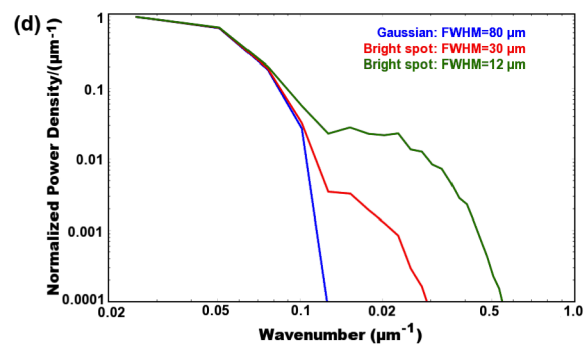
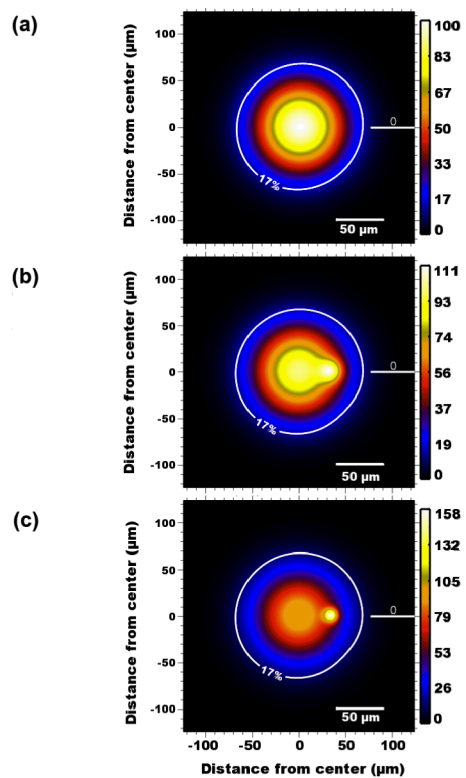
<sup>20</sup> T. Ma, N. Izumi, R. Tommasini, D.K. Bradley, P. Bell, C.J. Cerjan, S. Dixit, T. Döppner, O. Jones, J.L. Kline, G. Kyrala, O.L. Landen, S. LePape, A.J. Mackinnon, H.-S. Park, P.K. Patel, R.R. Prasad, J. Ralph, S.P. Regan, V.A. Smalyuk, P.T. Springer, L. Suter, R.P.J.

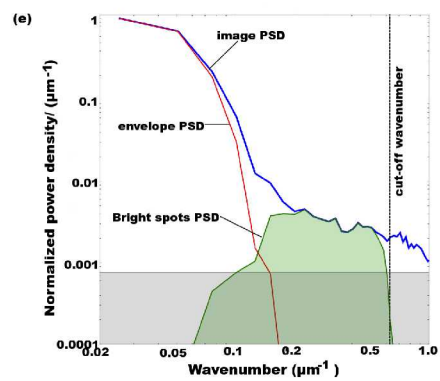
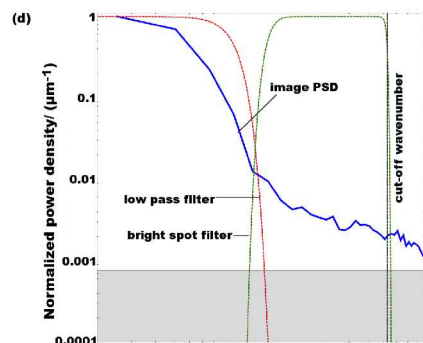
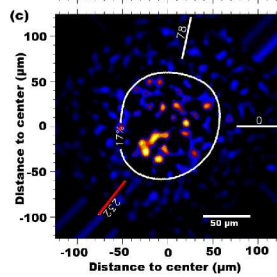
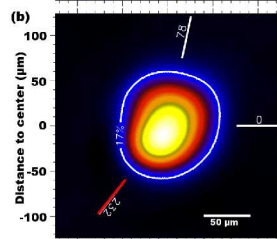
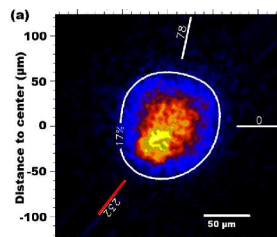
Town, S.V. Weber, and S.H. Glenzer, Review of Scientific Instruments **83**, 10E115 (2012).

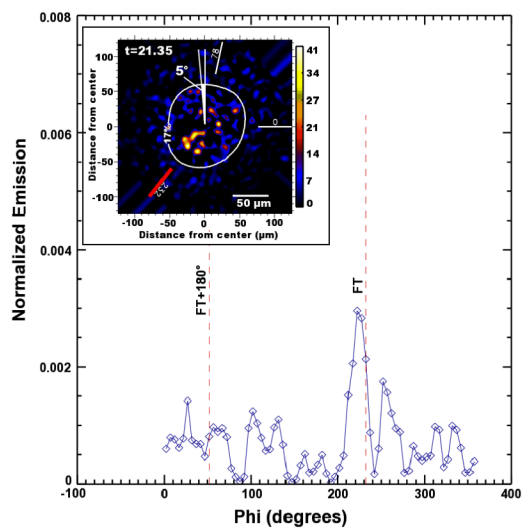
<sup>21</sup> B.A. Hammel, *Private Communication* (2011).

FIGURES

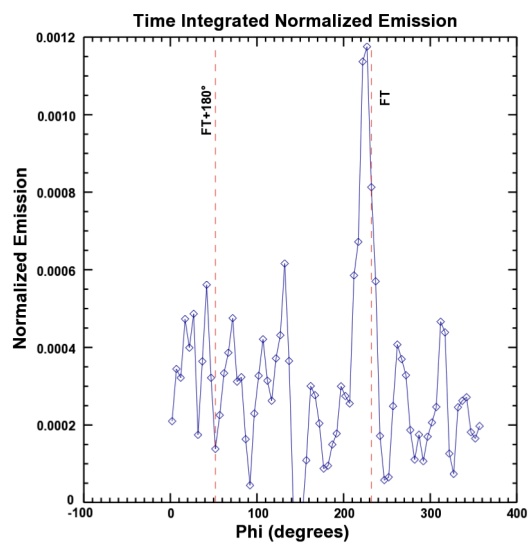


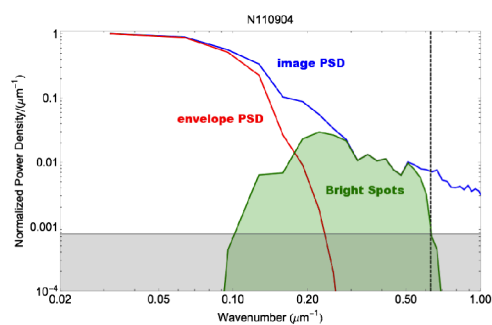
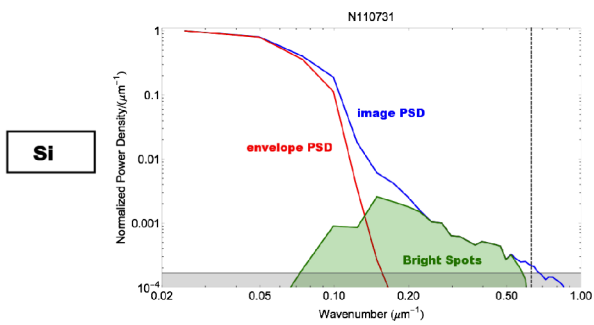
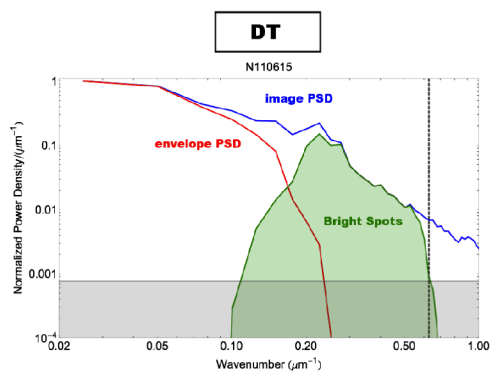
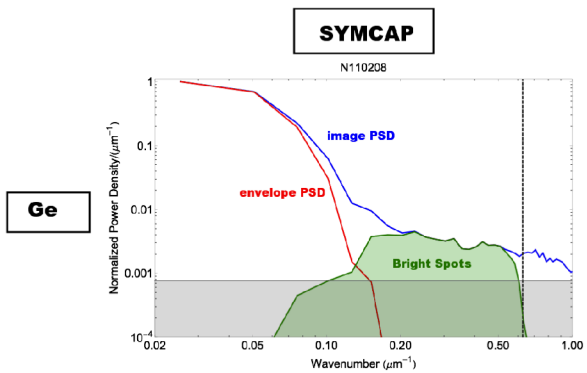


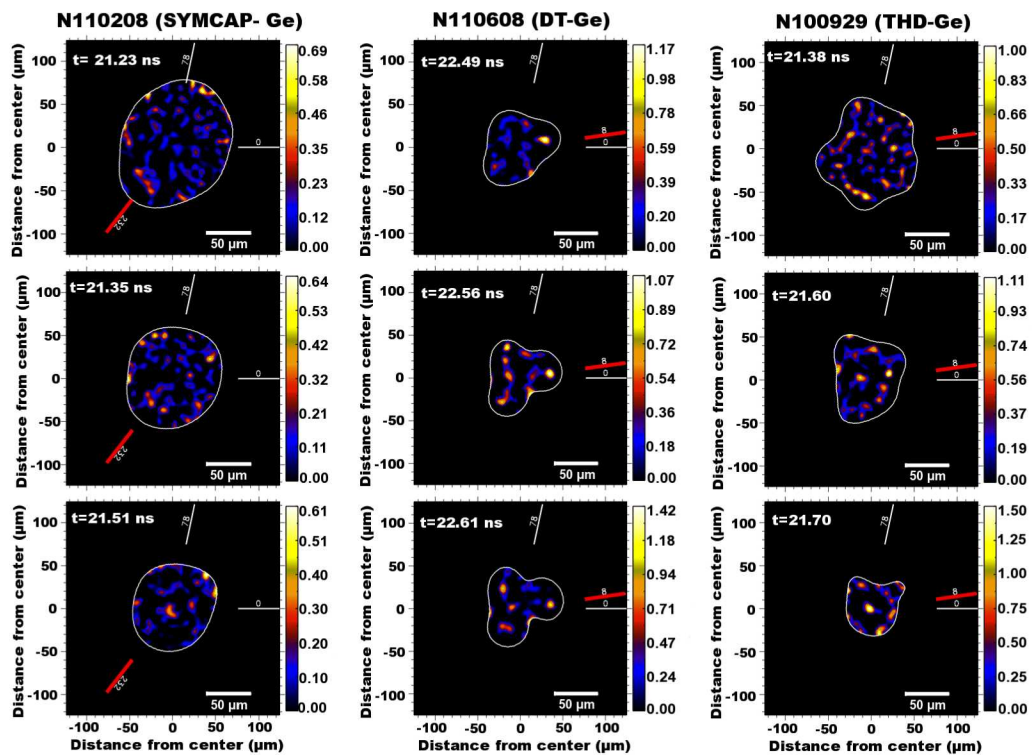












### Shot Averaged Time Integrated Normalized Emission

